Journal of Energy Chemistry 77 (2023) 180–190

Contents lists available at ScienceDirect

Journal of Energy Chemistry

journal homepage: www.elsevier.com/locate/jechem

http://www.journals.elsevier.com/journal-of-energy-chemistry/

A dilute fluorine-free electrolyte design for high-voltage hybrid aqueous batteries

Rui Lin [a,b], Jiahao Chen [a,b], Changming Ke [d,e], Shi Liu [d,e], Jianhui Wang [a,b,c,*]

[a] School of Materials Science & Engineering, Zhejiang University, Hangzhou 310024, Zhejiang, China
[b] Key Laboratory of 3D Micro/Nano Fabrication and Characterization of Zhejiang Province, School of Engineering, Westlake University, Hangzhou 310024, Zhejiang, China
[c] Institute of Advanced Technology, Westlake Institute for Advanced Study, Hangzhou 310024, Zhejiang, China
[d] Key Laboratory for Quantum Materials of Zhejiang Province, Department of Physics, School of Science, Westlake University, Hangzhou 310030, Zhejiang, China
[e] Institute of Natural Sciences, Westlake Institute for Advanced Study, Hangzhou 310024, Zhejiang, China

ARTICLE INFO

Article history:
Received 11 July 2022
Revised 17 October 2022
Accepted 23 October 2022
Available online 30 October 2022

Keywords:
High-voltage hybrid aqueous batteries
Fluorine-free electrolyte design
Interphase chemistry
Polyethylene glycol dimethyl ether

ABSTRACT

Fluorinated salts and/or high salt concentrations are usually necessary to produce protective films on the electrodes for high-voltage aqueous batteries, yet these approaches increase the cost, toxicity and reaction resistances of battery. Herein, we report a dilute fluorine-free electrolyte design to overcome this dilemma. By using the $LiClO_4$ salt and polyethylene glycol dimethyl ether (PED) solvent and optimizing the $LiClO_4$/PED/H_2O molar ratio, we formulate a 1 mol kg^{-1} 3 V-class hybrid aqueous electrolyte that enables reversible charge/discharge of 2.5 V $LiMn_2O_4$|$Li_4Ti_5O_{12}$ full cell at both low (0.5C, 92.4% capacity retention in 300 cycles) and high (5C, 80.4% capacity retention in 2000 cycles) rates. This excellent performance is reached even without the generation of protective film on either anode or cathode as identified by in/ex situ characterizations. The selection of appropriate ingredients that have both high stability and strong interactions with water is critical to widen the potential window of electrolyte while suppressing parasitic reactions on the electrodes. This work suggests that expensive and toxic fluorinate salts are no longer necessary for 3 V-class aqueous electrolytes, boosting the development of low-cost, environmentally-friendly, high-power and high-energy-density aqueous batteries.

1. Introduction

Safe and environment-friendly batteries are urgently in demand for the development of sustainable energy system. Aqueous lithium-ion batteries have attracted intense attention owing to their intrinsic safety, eco-environmental friendliness, facile manufacture and high power [1,2]. However, the energy density of the present aqueous batteries (e.g., lead-acid and Ni-Cd batteries) is less than one-third of that of conventional nonaqueous lithium-ion batteries, which dramatically decreases the market share of aqueous batteries. The low energy density of aqueous batteries is mainly attributed to the narrow electrochemical stability window (1.23 V) of water that excludes the utilization of most of high-capacity anodes and cathodes adopted in nonaqueous lithium-ion batteries (see Fig. 1 left). Recently, the electrochemical stability window of aqueous electrolytes is expanded to > 3 V by applying a salt-concentrated strategy and/or hybridizing with organic components, which effectively reduces the content of free-state water in aqueous electrolytes and endows robust electrolyte-electrode interphase (or protective film), and consequently, achieving an enhanced energy density closing to some nonaqueous lithium-ion batteries [3–9]. These above strategies quite rely on fluorinated salts, such as lithium bis(trifluoromethane sulfonyl)imide (LiTFSI), lithium trifluoromethane sulfonate (LiOTf) and lithium bis (pentafluoroethane sulfonyl)imide (LiBETI), for stable interphase formation. However, these fluorinated salts are expensive and toxic, and the produced protective film increases the battery internal resistance, which considerably undermines the merits of low cost, low toxicity and high power of aqueous batteries (Fig. 1 middle) [10].

Ideally, using cheap and fluorine-free salts, such as lithium polyacrylate (LiPAA), lithium acetate (LiAc), and lithium perchlorate ($LiClO_4$), instead of fluorinated salts can address the issues of cost and environmental hazards. However, in fluorine-free aqueous electrolytes, the electrode-electrolyte interphases are usually not stable enough to support a long-term operation of high-voltage aqueous batteries even under the condition of high salt

* Corresponding author.
E-mail address: wangjianhui@westlake.edu.cn (J. Wang).

https://doi.org/10.1016/j.jechem.2022.10.033

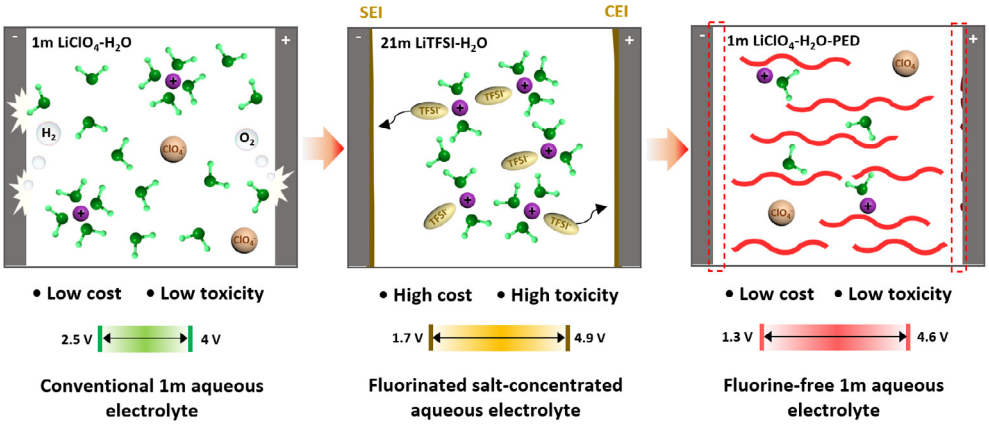

Fig. 1. Electrolyte design for dilute and fluorine-free high-voltage aqueous battery. Conventional dilute aqueous electrolyte shows a narrow electrochemical window, suffering from severe water decomposition when charging the battery at high voltages. Fluorinated salt-concentrated electrolyte (such as 21 m LiTFSI–H_2O) expands the electrochemical stability window because of the reduction of free-state water and the formation of protective electrode-electrolyte interphases mainly derived from $TFSI^-$ anion. However, the salt-concentrated strategy with fluorinated salt inevitably increases the cost and toxicity of electrolytes and the internal resistance of battery. This dilemma can be addressed by using the dilute fluorine-free aqueous electrolyte. The stable $LiClO_4$ salt and PED solvent are selected to regulate the hydrogen-bonding network and the molar ratio of $LiClO_4$:PED:H_2O is optimized to minimize the water activity. Consequently, this 1 mol kg^{-1} fluorine-free aqueous electrolyte achieves a wide electrochemical window of 3.3 V (1.3 ~ 4.6 V vs Li^+/Li) even without the aid of protective electrolyte–electrode interphases.

concentrations [11–14]. For a dual-salt concentrated aqueous electrolyte (32 m KAc—8 m LiAc in H_2O), a significant capacity decay was found in the 2.2 V $LiMn_2O_4$ (LMO)|TiO_2 full cell after 50 cycles [11,13]. For an aqueous/nonaqueous hybrid salt-concentrated electrolyte (5.7 m $LiClO_4$ in H_2O/Methylsulfonylmethane), the Coulombic efficiency (CE) was only 89.4% at 1C for the $Li_4Ti_5O_{12}$ (LTO) electrode, indicating it is difficult to support a stable charge/discharge operation at a moderate current density, let alone at a smaller one [11,13]. Most recently, the liquid polymer of polyethylene glycol (PEG) was reported to effectively suppress the hydrogen evolution reaction (HER) at a relatively low salt concentration of 2 m via altering the hydrogen-bonding network to reduce the water activity, thus widening the electrochemical stability window of aqueous electrolyte [15]. However, the PEG has poor oxidative stability because its terminal hydroxide group of —OH is readily oxidized at potentials above 4.1 V vs Li^+/Li [16], which would impair the long-term stability of high-voltage aqueous batteries. Therefore, it remains a challenge to develop low-cost, environmentally friendly (fluorine-free) and high-voltage aqueous electrolytes.

In this work, we selected the $LiClO_4$ salt and polyethylene glycol dimethyl ether solvent (PED, structurally similar to PEG but with a stable terminal group of $-OCH_3$) to formulate the aqueous electrolyte based on three aspects: (1) PED and $LiClO_4$, with electrochemical stability windows of 1 ~ 4.3 V vs Li^+/Li [16–18] and 1 ~ 4.6 V vs Li^+/Li [19–22], respectively, are both stable in the working potential range of the LMO|LTO battery (1.3 ~ 4.3 V vs Li^+/Li), avoiding adverse decomposition on the cathode/anode upon the charge and discharge; (2) Both PED and Li^+ cation can strongly interact with H_2O, which regulates the hydrogen-bonding network to reduce the activity of water, and thus, suppressing the decomposition of water during the cycling; (3) Both $LiClO_4$ and PED are inexpensive and fluorine-free, benefiting for the decrease of cost and toxicity of the electrolyte. By optimizing the molar ratios of $LiClO_4$: PED: H_2O, the content of free-state water in the electrolyte can be substantially reduced even at a dilute concentration of 1 m (Fig. 1 right). Finally, we obtained a 1 m fluorine-free aqueous electrolyte that enabled a stable charge/discharge operation of a 2.5 V LMO|LTO battery (150 Wh kg^{-1}) at both low and high rates, i.e., 92.4% capacity retention for 300 cycles at 0.5C and 80.4% capacity retention for 2000 cycles at 5C, without the generation of significant protective films on either anode or cathode.

2. Experimental

2.1. Electrolyte preparations

Lithium perchlorate ($LiClO_4$) and lithium bis(trifluoromethane sulfonyl) (LiTFSI) with a purity of > 99% were purchased from DodoChem (Suzhou). Polyethylene glycol dimethyl ether (PED 250, > 98%) and polyethylene glycol (PEG 250, > 98%) were purchased from LookChem (Shanghai). The $LiClO_4$/H_2O solutions were firstly prepared by dissolving the $LiClO_4$ salt into the deionized water (purified by Milli-Q from Millipore) with a given salt-to-H_2O molar ratio (1:10, 1:5, 1:3, 1:2) at ambient atmosphere. The PED-assisted electrolytes of 1 m Li—$10H_2O$—3.3PED, 1 m Li—$5H_2O$—3.6PED, 1 m Li—$3H_2O$—3.8PED and 1 m Li—$2H_2O$—3.9PED were prepared by introducing the PED into the above $LiClO_4$/H_2O solutions until the salt concentration reached 1 m. The compositions of as-prepared 1 m PED-assisted aqueous electrolytes are listed in Table S1. For comparison, aqueous electrolytes of 1 m Li—$56H_2O$, 6 m Li—$9H_2O$, 1 m Li—$2H_2O$—3.9PEG and 2 m LiTFSI—$1.7H_2O$—1.2PEG were prepared in the same way. Besides, a commercial nonaqueous electrolyte of 1 M $LiPF_6$ in ethylene carbonate/dimethyl carbonate (by vol 1:1) (1 M $LiPF_6$—EC/DMC) purchased from DodoChem (Suzhou) was also used as the reference.

2.2. Electrode preparations

$Li_4Ti_5O_{12}$ (LTO), $LiMn_2O_4$ (LMO), active carbon, acetylene black and polyvinylidene fluoride (PVDF) were purchased from Kejing Co. ltd (Shenzhen). The electrode materials of LTO and LMO have particle sizes of 5 ~ 20 μm and 10 ~ 25 μm, respectively (see Fig. S1), and they were used directly without any surface coating. The electrode slurry was prepared by mixing the active material, acetylene black and PVDF with a weight ratio of 8:1:1. Stainless-steel foil (SUS, 10 μm thickness) and Ti foil (10 μm thickness), purchased from Guangdong Canrd New Energy Technology Co. ltd,

were used as current collectors for the cathode and anode, respectively. The as-prepared electrodes were dried under vacuum at 120 °C for 4 h. The mass loadings of the LMO and LTO electrodes were 6 ∼ 8 and 4 ∼ 5 mg cm^{-2}, respectively.

2.3. Cell assembly and electrochemical measurements

Linear sweep voltammetry (LSV) and cyclic voltammetry (CV) measurements were carried out in a Swagelok three-electrode cell on a potentiostat (BioLogic, MPG-2) to evaluate the electrochemical stability window and reaction reversibility of the electrodes, respectively. The active carbon (mass loading: 8 ∼ 10 mg cm^{-2}) and Ag/AgCl (in saturated KCl solution, 3.239 V versus Li^+/Li) were used as the counter electrode and reference electrode, respectively. For LSV, the Ti and SUS electrodes were used as the working electrodes for the cathodic and anodic scans, respectively. The scanning rate was 5 mV s^{-1}. The onset potential of the electrochemical window was set at the current density of 0.05 mA cm^{-2}. For CV, the scanning rate of CV was 0.5 mV s^{-1}.

The full cells were assembled at ambinent atmosphere on a CR2032-type coin cell using the LMO cathode, LTO anode and glass fiber (Whatman, GF/D) separator. The negative/positive (N/P) capacity ratio was 0.8 ∼ 0.9. The amount of electrolyte in a coin cell was about 30 μL. A Ti foil was placed between the anode and battery case to minimize side reactions between the aqueous electrolyte and the SUS coin cell. Galvanostatic charge/discharge cycling and rate capability measurements were conducted on a battery test system (Neware, CT-4008) at 25 ℃. Charge and discharge were conducted at the same C-rate without using a constant-voltage mode at both ends of the charge and discharge. The capacity was calculated based on the total weight of positive and negative active materials. A 1C rate corresponds to 68 mA g^{-1} on the weight basis of all active materials from both the cathode and anode. The energy density of the full cell was calculated by the total weight of the cathode and anode.

2.4. Characterizations of solution structures

The hydrogen-bonding structures of aqueous solutions were characterized by a Fourier transform infrared spectrometer (FTIR, ThermoFisher iS50) with an attenuated total reflection (ATR) sample cell. All ATR-FTIR spectra were recorded in 32 scans with a resolution of 4 cm^{-1}. The coordination state of ClO_4^- anions in the solutions were evaluated by a Raman spectrometer (Anton Paar, Cora 5700) using a 785 nm laser.

2.5. Measurements of physical and chemical properties of electrolytes

The ionic conductivity of various solutions was measured in a symmetric Pt|electrolyte|Pt cell on an AC impedance spectroscopy (Solartron, 1470E) with a frequency range from 10^6 to 0.1 Hz and a potential amplitude of 10 mV. The viscosity was measured by a kinematic viscometer (Anton Paar, SVM 3001). Electrochemical impedance spectroscopy (BioLogic, MPG-2) of the LMO|LTO full cells at the half-discharge state (50% SOC) was tested on a frequency range from 20 kHz to 0.005 Hz with an AC amplitude of 10 mV. Self-extinguishing times of the electrolytes were determined in a flame test, in which the electrolyte-soaked glass fiber was ignited by a propane-oxygen torch burner.

2.6. Characterizations of materials' surface and morphology

The surface analysis of the cycled electrodes was conducted by an X-ray photoelectron spectrometer (XPS, ESCALAB Xi^+) with Al-*K*α X-ray source. The charge neutralizer was applied to compensate for the surface charge. All studied electrodes were subjected to a rinse by the DMC solvent and dried under vacuum before XPS measurements. The binding energy was calibrated using C 1 *s* peak at 284.8 eV. The morphology of the electrode materials was characterized by a field emission scanning electron microscope (FE-SEM, Gemini500) and transmission electron microscopy (TEM, Talos F200X G2).

2.7. In situ ATR-FTIR measurements

In situ ART-FTIR measurements were carried out in a crafted two-electrode cell that was fixed on the sample stage of ATR (PIKE, VeeMAX III). The LMO or LTO electrode was pressed on the diamond crystal for study. On a potentiostat (IVIUM, OctoStat200), the LMO|LTO full cell was charged and discharged at a 1C rate. During the initial two charge-discharge cycles, FTIR spectra were collected to reveal the formation process of protective films on the studied LMO or LTO electrode. All spectra were recorded in 32 scans with a resolution of 4 cm^{-1}.

2.8. In situ DEMS measurements

In situ DEMS measurements were applied to detect hydrogen and oxygen gases generated on the assembled Swagelok cells that were connected to a quadrupole mass spectrometer (QAS 100, Shanghai Linglu). The charge/discharge tests of the LMO|LTO full cell with different electrolytes were controlled by a potentiostat (IVIUM, OctoStat200). Before the DEMS measurement, pure Ar was flushed to remove the air for 2 h.

2.9. Simulations

The solution structure was theoretically investigated by Vienna *ab initio* simulation package (VASP), a software for performing *ab initio* molecular dynamics (MD) simulation using a plane wave basis set. The projector augmented wave method was used for electronic structure calculations. The exchange–correlation interaction was described by PBE functionals with D3 dispersion correction from Grimme. The cutoff energies and electronic energy self-consistency criteria were set to 380 eV and 10^{-6} eV, respectively. The solution of $1LiClO_4$–$2H_2O$–4PED was calculated in a cubic supercell with a lattice constant of 12 Å. The gamma point was only used to sample the Brillouin zone in MD simulations. The temperature of *NVT* ensemble was controlled using the Nose-hoover thermostat. The solution was first equilibrated at a higher temperature (698 K, 5 ps) to generate a configuration with fully mixed solvents and solutes. The high-temperature equilibrated solution structures were then used as the initial configuration of the MD simulation with a longer time (15 ps) at room temperature.

3. Results and discussion

3.1. Preparation and characterization of dilute fluorine-free aqueous electrolytes

A series of aqueous solutions with different molar ratios of $LiClO_4$: PED: H_2O were prepared in an ambient atmosphere. The concentration of $LiClO_4$ salt is 1 m and the compositions of the solutions are listed in Table S1. For convenience, the aqueous solutions are named as 1 m Li–*x*H_2O–*y*PED, wherein *x* and *y* correspond to the molar ratio of H_2O-to-$LiClO_4$ and PED-to-$LiClO_4$, respectively. For comparison, the $LiClO_4$–H_2O solutions with different salt concentrations were also prepared for study.

As shown in Fig. 2(a) and Fig. S2, H—O stretching vibration (3200 ∼ 3700 cm^{-1}) in different solutions was characterized by Fourier Transform infrared (FTIR) spectroscopy. The absorbance

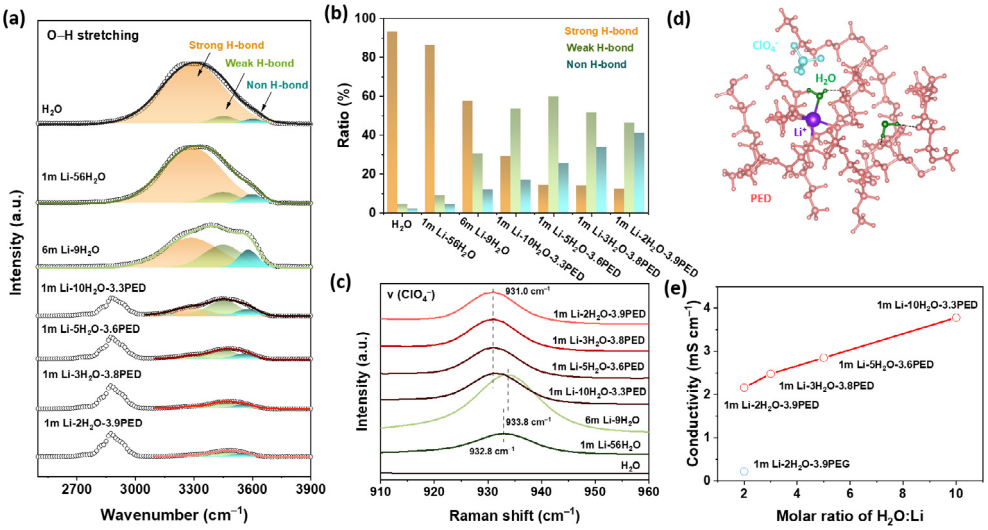

Fig. 2. Characterizations of aqueous solutions dependent on the PED content. (a) FTIR spectra of various PED-assisted aqueous solutions (1 m Li–$x$$H_2O$–$y$PED, x and y correspond to the H_2O-to-$LiClO_4$ and PED-to-$LiClO_4$ molar ratio). (b) The contents of different hydrogen-bonding components in as-prepared aqueous solutions. (c) Raman spectra of as-prepared aqueous solutions in the range of 910 ~ 960 cm^{-1} (ClO_4^- stretching mode). (d) A snapshot of a typical equilibrium trajectory of 1 m $LiClO_4$–$2H_2O$–4PED electrolyte during *Ab initio* MD (AIMD) simulations. The dashed line represents the hydrogen bond. (e) Ionic conductivities of various PED-assisted aqueous solutions at 25 °C. Pure water, (dilute 1 m and saturated 6 m) $LiClO_4$–H_2O solutions and 1 m Li–H_2O–3.9PEG were used as references.

peaks at ~3290, ~3450 and ~3600 cm^{-1} correspond to water molecules with strong hydrogen-bond (SHB), weak hydrogen-bond (WHB) and non-hydrogen-bond (NHB), respectively [23]. To quantify the contents of water molecules in different states, we deconvoluted the FTIR absorbance peaks and the calculated results are shown in Fig. 2(b) and Fig. S2. The introduction of either $LiClO_4$ or PED in water can significantly decrease the content of SHB, indicating both the $LiClO_4$ and PED have the capability of regulating hydorgen-bonding network. For the pristine $LiClO_4$–H_2O solutions without PED, when the salt concentration increased from 1 m to saturated 6 m, the formation of contact-ion-pairs (CIPs) and/or aggregates (AGGs) further decreased the content of free-state water, however, the content of SHB component remained the major part (~60%) even in the saturated concentration. By contrast, when both $LiClO_4$ and PED were added to the water, the content of SHB can be dramatically decreased to < 30% even at a dilute concentration of 1 m Li–$10H_2O$–3.3PED, evidencing strong interactions among the H_2O, $LiClO_4$ and PED that break the hydrogen-bonding network of water. When the content of PED increased, the SHB components further decreased and the WSB and NSB components became dominant at y > 3.6 (> 80%). In the 1 m Li–$2H_2O$–3.9PED, the SHB components almost disappeared, indicating that the content of free-state water is substantially reduced in this solution. The states of ClO_4^- in solution were characterized by Raman spectroscopy. As shown in Fig. 2(c), the Cl–O symmetric stretching vibration of ClO_4^- ion in 1 m $LiClO_4$–$56H_2O$ solution positioned at 932.8 cm^{-1}, which blueshifted to 933.8 cm^{-1} in 6 m $LiClO_4$–$9H_2O$ solution because the ClO_4^- anion participated in the coordination to Li^+ with the formation of CIPs and/or AGGs. By contrast, in the 1 m PED-assisted electrolytes, the Raman peak of ClO_4^- anion had a slight redshift as compared to that of the 1 m $LiClO_4$–$56H_2O$ solution, indicating that ClO_4^- anions existed in a free state with no coordination to either Li^+ or PED.

To understand how the interactions among H_2O, Li^+ and PED regulate the hydrogen-bonding network of water, we carried out *Ab initio* MD (AIMD) simulation to investigate the solvation structure of the 1 m Li–$2H_2O$–3.9PED solution. Fig. 2(d) shows a snapshot of a typical equilibrium trajectory of the solution during AIMD simulations. Clearly, PED and water molecule are in the primary solvation sheath of Li^+. Typically, one Li^+ coordinates with one H_2O and two PED molecules via Li···O interaction. Besides, the other H_2O interacts with the left PED through hydrogen bond (H(H_2O)···O (PED)). In this way, the strong hydrogen-bonding network of water is cut off and the water activity is effectively reduced in the solution of 1 m Li–$2H_2O$–3.9PED. For the ClO_4^-, we found it keeps in a free state during the simulation, consistent with the Raman results.

According to FTIR, Raman and AIMD results, it is clear that the PED is tightly coordinated to H_2O and Li^+ cation but rather than to ClO_4^-. The strong interactions among H_2O, Li^+ and PED not only effectively reduce the water activity but also suppress the volatility of the dilute electrolyte. From a thermogravimetric test (see Fig. S3 and Table S2), the weight loss of 1 m Li–$2H_2O$–3.9PED was only −3.1 wt% upon heating to 100 °C, which is 20 times lower than that of 1 m Li–$56H_2O$ (−65.4 wt%). Because the PED is flammable, the 1 m Li–$2H_2O$–3.9PED hybrid aqueous electrolyte has a self-extinguishing time of 30 s g^{-1}, which is slightly shorter than the PEG-based electrolytes (see Table S2). On the other hand, the presence of free-state ClO_4^- anion in the unique solvation structure of 1 m Li–$2H_2O$–3.9PED promotes the dissociation of $LiClO_4$ salt in the solution. The ionic conductivity of 1 m Li–$2H_2O$–3.9PED solution reached 2.1 mS cm^{-1} at room temperature, which is nearly an order of magnitude higher than that of 1 m Li–$2H_2O$–3.9PEG (0.22 mS cm^{-1}) (see Fig. 2e), and also significantly higher than most reported polymer-based solid/quasi-solid electrolytes, benefiting for a fast charge/discharge operation of batteries.

3.2. Electrochemical properties of fluorine-free aqueous electrolytes

The electrochemical stability windows of various solutions were evaluated by linear sweep voltammetry (LSV). Stainless steel (SUS) and titanium (Ti) foils were used as the working electrodes to test the anodic and cathodic potential limits, respectively. The onset current density for the electrochemical stable window was set as 0.05 mA cm^{-2}. As shown in Fig. 3(a), the electrochemical stability window of 1 m Li–$56H_2O$ was only 1.8 V, which increased to 2.1 V by increasing the salt concentration from 1 m to 6 m. Alternatively, the introduction of PED remarkably widened the electrochemical stability window to 2.6 V with the lower and upper potential limits at 1.8 and 4.4 V vs Li^+/Li, respectively, even in a

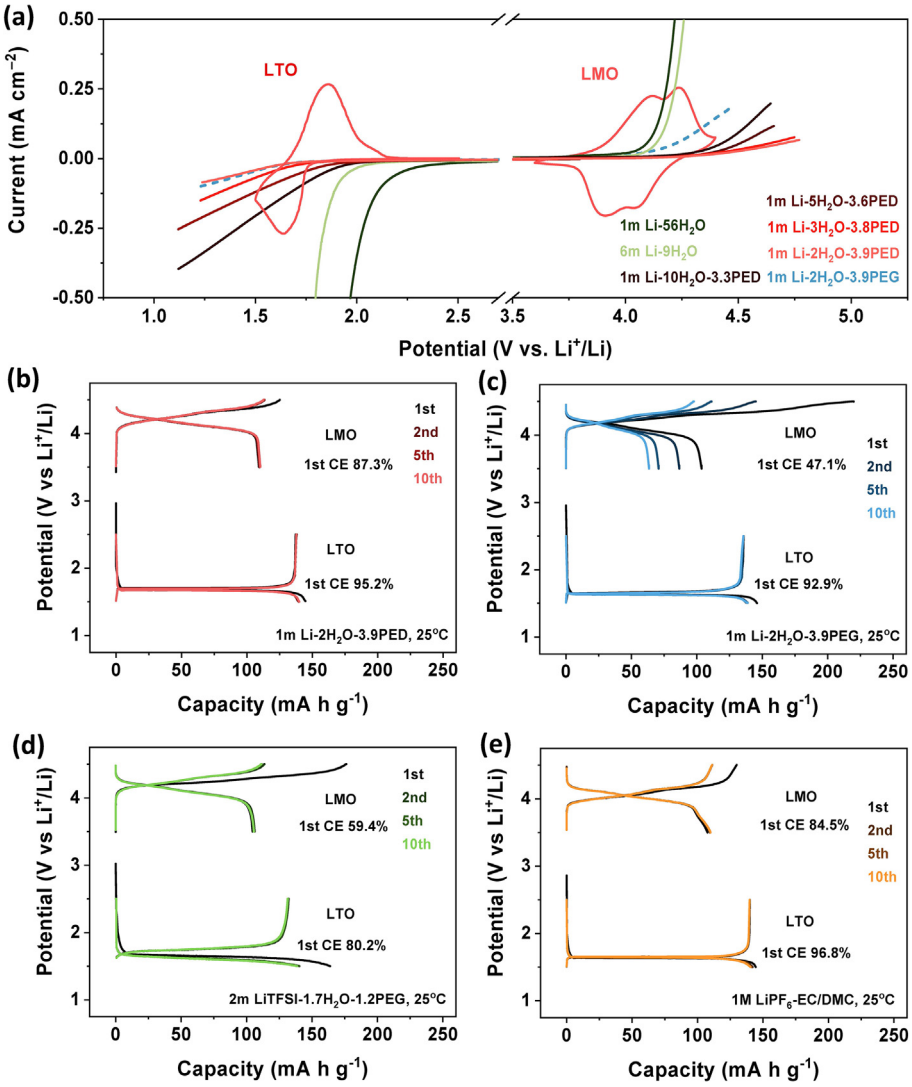

Fig. 3. Compatibility tests of as-prepared aqueous electrolytes with various electrodes. (a) LSV curves of different aqueous electrolytes: Ti and stainless steel (SUS) were used as the working electrodes for the cathodic and anodic scans, respectively. CV curves of the LTO and LMO electrodes in the electrolyte of 1 m Li−2H_2O−3.9PED were also presented. Charge/discharge curves of LMO and LTO electrodes in three-electrode cells using aqueous electrolytes of 1 m Li−2H_2O−3.9PED (b), 1 m Li−2H_2O−3.9PEG (c) and 2 m LiTFSI−1.7H_2O−1.2PEG (d), and a nonaqueous electrolyte of 1 M $LiPF_6$−EC/DMC (e). The active carbon and Ag/AgCl electrodes were used as the counter electrode and the reference electrode, respectively. A 1C rate corresponds to 170 mA g^{-1} for the cell using the LTO working electrode, and to 140 mA g^{-1} for the cell using the LMO working electrode, respectively.

dilute solution (1 m Li−10H_2O−3.3PED), evidencing the role of PED in stabilizing the water. When optimizing the PED/H_2O molar ratio to decrease the water content in the solution (1 m Li−2H_2-O−3.9PED), the electrochemical stability window further expanded to 3.3 V (1.3 ∼ 4.6 V vs Li^+/Li), which enabled a fully reversible Li^+ intercalation/de-intercalation of both LTO and LMO electrodes. Similar to 1 m Li−2H_2O−3.9PED, the electrolyte of 1 m Li−2H_2O−3.9PEG also allowed reversible Li^+ intercalation/de-intercalation of LTO electrode. However, due to the poor oxidative stability of the terminal group of −OH, this PEG-assisted electrolyte only showed an upper potential limit at 4.1 V vs Li^+/Li, which cannot support a stable charge/discharge operation of the LMO electrode. The poor oxidation stability of PEG can be solved via the usage of the fluorinated salt and high salt concentration, which endows protective films on the electrodes to suppress the continuous decomposition of PEG. In the case of 2 m LiTFSI−1.7H_2-O−1.2PEG, the generation of protective films during the first LSV scan extended the lower and upper potential limits to ∼1.2 and 4.8 V vs Li^+/Li, respectively (see Fig. S4). However, this approach also significantly increases the cost and toxicity of the electrolyte. By contrast, our electrolyte of 1 m Li−2H_2O−3.9PED successfully expanded the electrochemical stability window without compromising the cost and toxicity. Interestingly, the first and second LSV curves were almost identical for the fluorine-free PED-assisted electrolyte, implying that no protective films have been generated during the LSV scans.

To confirm the compatibility between the as-prepared electrolytes and the LMO and LTO electrodes, we carried out the charge/discharge operation in a three-electrode cell with the LMO (or LTO), active carbon and Ag/AgCl as the working, counter and reference electrode, respectively. As shown in Fig. 3(b and c), both the PED- and PEG-assisted electrolytes can support reversible Li^+ de-/intercalation of the LTO electrode. However, for the LMO electrode, an apparent oxidation reaction in the PEG-assisted electrolyte occurred at voltages > 4.2 V in the first charge process with a poor initial CE of < 50% (Fig. 3c). The electrolyte of 2 m LiTFSI−1.7H_2O−1.2PEG enabled reversible charge/discharge reactions of both LMO and LTO (Fig. 3d). However, the initial anodic

and cathodic CEs were 59.4% and 80.2%, respectively, which are considerably lower than those (87.3% and 95.2%) using the fluorine-free 1 m Li−$2H_2O$−3.9PED electrolyte. It is well-known that the commercial LMO|LTO batteries using nonaqueous electrolytes do not generate compact protective films on the electrodes because the redox potentials of LMO (1.3 V vs SHE) and LTO (−1.5 V vs SHE) locate within the electrochemical stability window of the nonaqueous carbonate ester electrolyte [24–27]. Compared to the LMO|LTO battery using the nonaqueous electrolyte of 1 M $LiPF_6$−EC/DMC (initial anodic CE 84.5%, cathodic CE 96.8%, see Fig. 3e), the one using 2 m LiTFSI−1.7H_2O−1.2PEG demonstrates considerably lower initial CEs, indicating that protective films have formed on the electrodes, whereas, the one using 1 m Li−$2H_2O$−3.9PED shows comparable initial CEs, indicating that no such protective films have formed on the electrodes.

In this study, the initial anodic and cathodic CEs are not very high in the nonaqueous electrolyte of 1 M $LiPF_6$−EC/DMC and our dilute fluorine-free electrolyte of 1 m Li−$2H_2O$−3.9PED. The reason may be related to the electrode materials themselves, which are used as received without any surface treatment. Some parasitic reactions may occur between the chemically active spots of the electrode and the electrolyte, which decrease the initial CEs but don't contribute to the formation of continuous and compact protective interphase on the electrode surface (see Fig. 1). Qian et al. reported that the surface of LTO particles is usually aggregated by some impurities and defects during the material synthesis, which can induce side reactions with the electrolytes, causing a low initial CE of 88.5% [28]. Moreover, our results of initial CEs are consistent with much literature about LMO [29–33] and LTO [34–38], respectively. In addition, we examined the gas generation during the first charge/discharge cycle by in situ differential electrochemical mass spectrometry (in situ DEMS) and found very little hydrogen production (see Fig. S5).

We then tested the electrolytes in the 2.5 V LMO|LTO full cells (N/P = 0.8 ∼ 0.9 and 30 μL electrolyte). The rate and cycling performances are demonstrated in Fig. 4 and Fig. S6. Using 1 m Li−$2H_2O$−3.9PED electrolyte, the reversible capacity of the aqueous full cell was above 60 mA h g^{-1} (based on the total weight of LMO and LTO electrodes) at 0.5 ∼ 1C, which corresponds to ∼ 90% of theoretic capacity. Even at a high rate of 5C, the reversible capacity remained 36 mA h g^{-1}, indicating a good rate capability using the PED-assisted aqueous electrolyte (Fig. 4a). Moreover, this PED-assisted electrolyte also enabled a stable cycling operation at both low and high rates: at 5C, the capacity retention and average CE reached 80.4% and 99.1% in 2000 cycles, respectively; even at a small current density of 0.5C, the capacity retention and average CE reached 92.4% and 93.5% in 300 cycles, respectively (see Fig. 4c and d). The CE of 93.5% reflects the existence of some parasitic reaction in the battery at a small current density. This parasitic reaction is likely the corrosion of the current collector as previously reported in literature [7,10] but rather than a hydrogen evolution reaction because the latter will consume the electrolyte quickly and cannot support a long-term cycling with a limited amount of electrolyte (30 μL). By sharp contrast, the battery using 1 m Li−$2H_2O$−3.9PEG electrolyte showed a very poor rate capability and cycling durability: the reversible capacity was only 30 and 16 mA h g^{-1} at 2C and 3C, respectively (Fig. 4b); the capacity declined very fast within 10 cycles together with a very low CE of < 50% at either low (0.5C) and high (5C) rates (Fig. 4c and d). These above results firmly confirm that our dilute fluorine-free electrolyte design enables a fast-rate and stable 2.5 V aqueous Li-ion battery.

3.3. Internal resistances of the fluorine-free aqueous battery

To understand the kinetic property, we studied the internal resistances of batteries using different electrolytes. Generally, the Li^+ intercalation process involves three main resistances, which are Li^+ transport in the electrolyte (R_{elyt}), Li^+ charge transfer at the electrolyte-electrode interphases (R_{ct}), and Li^+ transport in the electrolyte-electrode interphases (R_{inter}) [26]. To evaluate these resistances in the LMO|LTO aqueous battery, we carried out electrochemical impedance spectroscopies (EIS) at a half-discharge state (50% SOC) during the first 20 cycles (Fig. S7). The Nyquist plots of the LMO|LTO full cells using different electrolytes and the equivalent circuit are exhibited in Fig. 5(a and b), respectively.

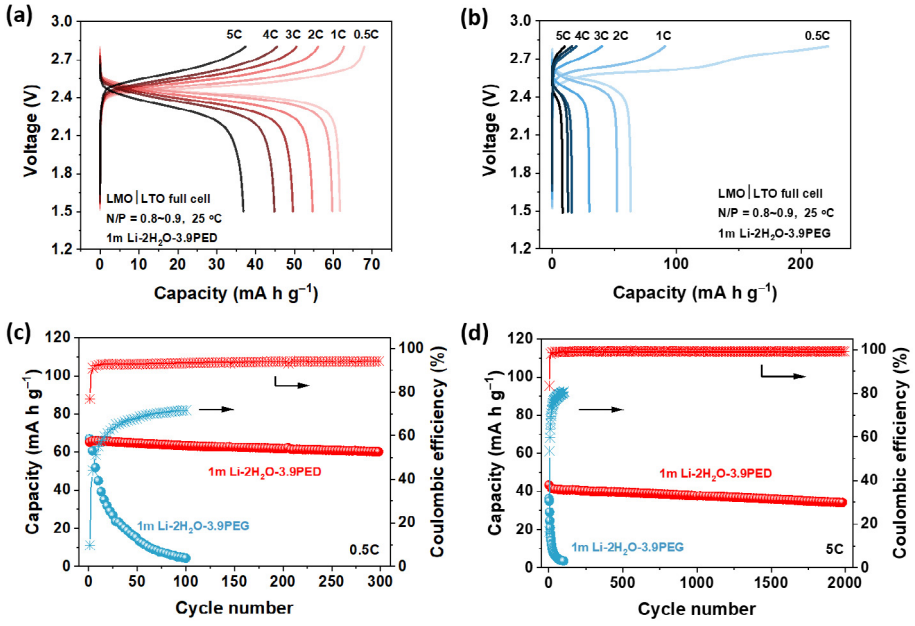

Fig. 4. Rate and cycling performances of LTO|LMO full cells using PED- and PEG-assisted aqueous electrolytes. (a and b) Charge/discharge profiles of the LTO|LMO full cells at different rates. (c and d) Cycling performance and Coulombic efficiency of the LMO|LTO full cells at 0.5C and 5C, respectively. Charge and discharge were conducted at the same C-rate with a cut-off voltage of 1.5 ∼ 2.8 V at 25 °C. The capacity was calculated based on the total weight of positive and negative active materials.

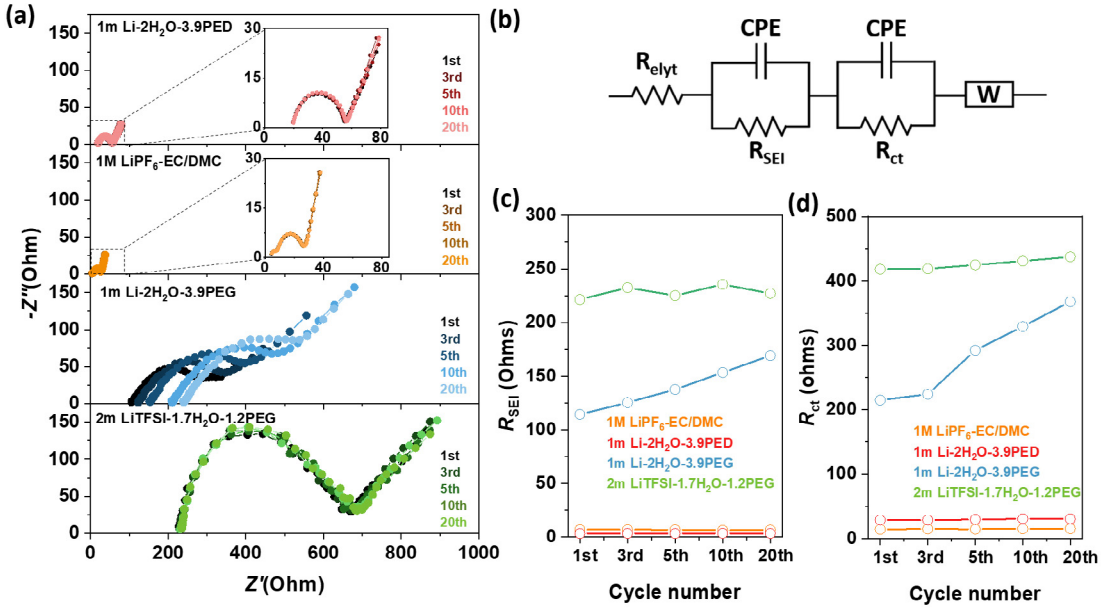

Fig. 5. Electrochemical resistance analysis of LMO|LTO batteries using different aqueous electrolytes. (a) Electrochemical impedance spectroscopies of the LMO|LTO batteries using aqueous (1 m Li−$2H_2O$−3.9PED, 1 m Li−$2H_2O$−3.9PEG, 2 m LiTFSI−1.7H_2O−1.2PEG) and nonaqueous (1 M $LiPF_6$−EC/DMC) electrolytes upon cycling. (b) Equivalent circuit for the LMO|LTO batteries. (c and d) Variances of calculated R_{ct} and R_{inter} upon cycling.

A typical EIS fitting is shown in Fig. S8 and the calculated resistances based on the equivalent circuit are summarized in Table S3 and plotted in Fig. 5(c and d). It is clear that, for the battery using the 1 m Li−$2H_2O$−3.9PED electrolyte, R_{elyt}, R_{ct} and R_{inter} were evaluated as 18.6, 28.8, and 3.1 Ω, respectively, which keep almost unchanged during the cycling, confirming a very stable electrochemical impedance. By sharp contrast, for the battery using the 1 m Li−$2H_2O$−3.9PEG electrolyte, R_{elyt}, R_{ct} and R_{inter} at 1st cycle were evaluated as 106.1, 214.9, and 114.2 Ω, respectively, which dramatically increased to 239.9, 367.8, and 169.1 Ω after 20 cycles. Such an unstable electrochemical impedance should result from the continuous oxidation of PEG on the cathode surface (Fig. 3c and S7b). It is worth noting that the R_{inter} (3.1 Ω) in 1 m Li−$2H_2O$−3.9PED electrolyte is very small as compared to the R_{elyt} (18.6 Ω) and R_{ct} (28.8 Ω), showing a negligible resistance for Li^+ transport in the electrolyte-electrode interphases. This characteristic is very similar to the SEI-free LMO|LTO battery using the nonaqueous electrolyte of 1 M $LiPF_6$−EC/DMC (R_{elyt} 3.6, R_{ct} 15.4, R_{inter} 4.7 Ω), intrinsically different from that in the reference electrolyte of 1 m Li−$2H_2O$−3.9PEG or previously reported molecular crowding electrolyte of 2 m LiTFSI−1.7H_2O−1.2PEG, both of which encounter a considerably larger R_{inter}. For 2 m LiTFSI−1.7H_2O−1.2PEG, the issue of unstable PEG is addressed via the formation of compact protective interphases on the electrodes. However, it brings about a new problem of increased Li^+ transport resistances (R_{ct} 418.1, R_{inter} 221.4 Ω) that severely compromise the rate capability, let alone the cost and toxicity issues. Overall, the introduction of PED leads to an expanded electrochemical stability window, a negligible R_{inter}, and a small yet stable total internal resistance, contributing to the development of a stable high-voltage LMO|LTO hybrid aqueous battery without compromising the properties of cost, toxicity and rate.

3.4. Electrolyte-electrode interphases of the fluorine-free aqueous battery

The electrolyte-electrode interphase profoundly affects the battery performances. To check if any electrolyte-electrode interphase is produced in the battery using the as-prepared aqueous electrolytes, we applied in situ attenuated total reflectance Fourier transform infrared (in situ ATR-FTIR) spectroscopy to monitor the changes on the surface of both cathode and anode during the initial two charge/discharge cycles (see Fig. 6 and Fig. S9). For the LMO|LTO battery using 1 m Li−$2H_2O$−3.9PEG electrolyte, two new IR absorbance peaks at around 1647 cm^{-1} (C═O) and 3060 ∼ 3670 cm^{-1} (O—H) appeared on the LMO surface at the voltages of > 2.5 V (see Fig. 6a), which can be attributed to the formation of PEG-carboxylic acid (named as R−COOH(Li)) caused by the oxidation of PEG [39,40]. This oxidative product likely adhered on the surface of ATR crystal, which causes the decrease of electrolyte concentration around the ATR crystal and brings a counter-absorbance of IR signal at around 844 and 1020 cm^{-1}. A similar phenomenon was also reported previously [8]. Whereas on the LTO surface, no IR absorbance can be detected, indicating that no significant reduction products were generated on the LTO surface during the charge/discharge process (see Fig. 6b). For the LMO|LTO battery using the 1 m Li−$2H_2O$−3.9PED electrolyte, we did not observe any IR signal on the surface of either LMO or LTO during the whole charge/discharge process (Fig. 6c and d), indicating that both of the two electrodes kept stable in the electrolyte and no interphase reaction occurred.

Moreover, we carried out X-ray photoelectron spectroscopy (XPS) measurements to study the chemical composition of the surface of the cycled electrodes (shown in Fig. 7 and Fig. S10). For comparison, the pristine and the electrolyte-soaked LMO and LTO electrodes were used as references. Consistent with the results of in situ ATR-FTIR, only the oxidation product of PEG was observed on the surface of the LMO electrode cycled in the 1 m Li−$2H_2O$−3.9PEG electrolyte and no significant oxidation or reduction products can be observed on the other electrodes. Besides, we also studied the LMO and LTO electrodes before and after cycling by transmission electron microscopy (TEM, Fig. S11 and Fig. S12), by which we did not observe a significant protective film on the electrode surface either. All these results above evidence that the fluorine-free electrolyte of 1 m Li−$2H_2O$−3.9PED does not contribute to significant protective film on either LMO or LTO in battery operation. Hence, the selection of appropriate ingredients with both high stability and high regulation capability of the

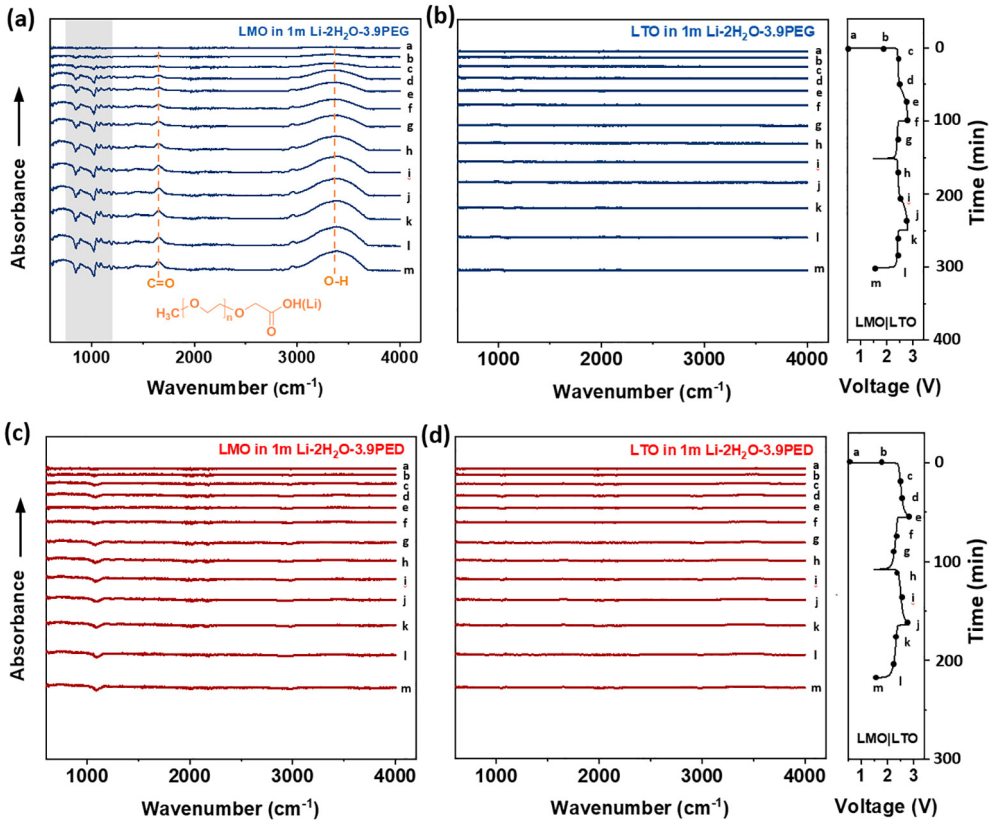

Fig. 6. In situ ATR-FTIR observations on the surface of the LMO and LTO electrodes in PED- and PEG-assisted aqueous electrolytes. (a) FTIR spectra of the LMO surface in the PEG-assisted electrolyte, (b) FTIR spectra of the LTO surface in the PEG-assisted electrolyte, (c) FTIR spectra of the LMO surface in the PED-assisted electrolyte, and (d) FTIR spectra of the LTO surface in the PED-assisted electrolyte. In situ ATR-FTIR measurements were carried out in the LMO|LTO full cells during the initial two charge/discharge cycles. Only PEG-carboxylic acid (R−COOH(Li)) was detected on the LMO electrode surface in the electrolyte of 1 m Li−2H_2O−3.9PEG, which is ascribed to the oxidation of PEG at high voltages.

hydrogen-bonding network is vital for the dilute fluorine-free aqueous electrolyte design.

3.5. Cost merit of the dilute fluorine-free aqueous electrolyte

The cost is one of the most important parameters for large-scale applications. Both the $LiClO_4$ salt and PED polymer are inexpensive, showing the good merit of cost for our designed dilute flurorine-free aqueous electrolyte. Compared to LiTFSI, the most widely used salt in high-voltage aqueous electrolytes, the price of $LiClO_4$ is reduced by > 84%. Moreover, the content of $LiClO_4$ salt in our 1 m Li−2H_2O−3.9PED electrolyte is only 9.5 wt%, which is considerably lower than those of the reported salt-concentrated aqueous or hybrid aqueous electrolytes (36 ~ 86 wt%) [4–6,9,15,41–45]. To the best of our knowledge, this is the lowest one among all the reported 3 V-class aqueous electrolytes. We assess the price of the aqueous electrolytes based on Chinese market quotations (see Table S4, 5). As shown in Fig. 8, the price of our 1 m Li−2H_2-O−3.9PED electrolyte is estimated to be 5500 USD ton^{-1}, which is only one 18th of the salt-concentrated electrolyte of 21 m LiTFSI−2.6H_2O and one 8th of the molecular crowding electrolyte of 2 m LiTFSI−1.7H_2O−1.2PEG. Even compared with the commercial nonaqueous electrolyte of 1 M $LiPF_6$−EC/DMC (~15000 USD ton^{-1}), our dilute fluorine-free electrolyte also demonstrates an obvious advantage in the cost. In addition, the high-voltage aqueous Li-ion batteries are manufactured at an ambient atmosphere with no need for high-energy-consuming dry rooms. This feature unique to the aqueous batteries will further reduce the cost considerably, promoting their large-scale applications.

4. Conclusions

We have developed a dilute fluorine-free hybrid aqueous electrolyte of 1 m Li−2H_2O−3.9PED with an electrochemical stability window of 3.3 V. This electrolyte design relies on the usage of stable $LiClO_4$ salt and PED solvent to regulate the hydrogen-bonding network. Owing to strong interactions among PED, Li^+ cation and H_2O, the water activity of the PED-assisted aqueous electrolytes is efficiently reduced via optimizing the molar ratio of $LiClO_4$: PED: H_2O even at the dilute salt concentration of 1 m, by which the parasitic reactions of water and other ingredients on the electrode surface are effectively suppressed. Using this new electrolyte, the 2.5 V LMO|LTO battery realized a stable charge/discharge cycling at both low and high rates: 92.4% capacity retention over 300 cycles at 0.5C and 80.4% capacity retention over 2000 cycles at 5C. The EIS analysis revealed that this battery has a very small internal resistance that is comparable with that of the well-known SEI-free LMO|LTO battery using the nonaqueous electrolyte of 1 M $LiPF_6$−EC/DMC, which accounts for a good rate capability. In situ ATR-FTIR and XPS characterizations further confirmed that no significant protective film is generated on the surface of either LMO or LTO in the battery using the dilute and fluorine-free electrolyte of 1 m Li−2H_2O−3.9PED, which is intrinsically distinguished from the reported salt-concentrated aqueous electrolytes and molecular crowding electrolytes. Hence, the expensive and toxic fluorinated salt is no longer necessary in a 3 V-class aqueous electrolyte design. Moreover, owing to the low cost and low toxicity of $LiClO_4$ and PED, our electrolyte exhibits remarkable advantages in the cost and environment-friendliness

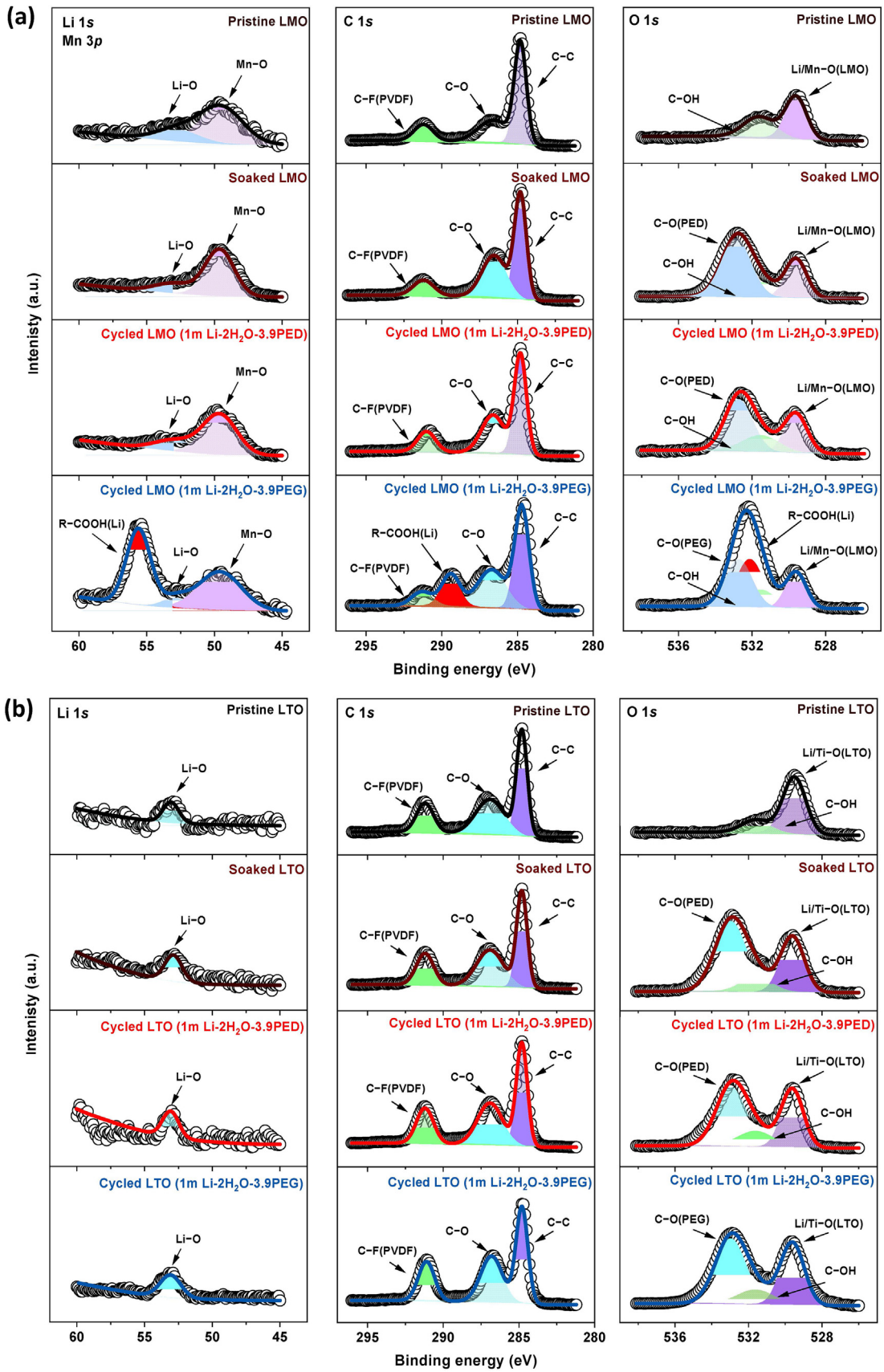

Fig. 7. XPS analysis of the surfaces of the LMO and LTO electrodes cycled in PED- and PEG-assisted aqueous electrolytes. (a) XPS spectra of the LMO electrodes cycled in PED- and PEG-assisted aqueous electrolytes. (b) XPS spectra of the LTO electrodes cycled in PED- and PEG-assisted aqueous electrolytes. The pristine and the electrolyte-soaked LMO and LTO electrodes were used as references. Only PEG-carboxylic acid was detected on the cycled LMO electrode in the PEG-assisted aqueous electrolyte.

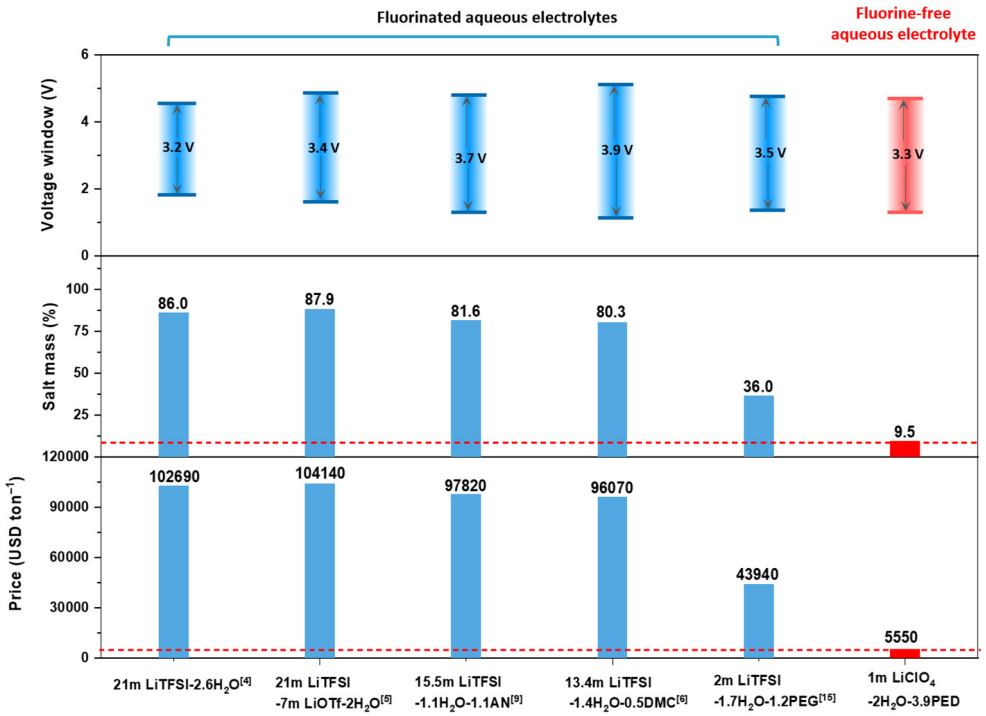

Fig. 8. Comparison of our fluorine-free aqueous electrolyte with other 3 V-class aqueous electrolytes previously reported. The price of various aqueous electrolytes was estimated based on the information from Chinese market quotations as listed in Table S3 and Table S4.

among the reported 3 V-class aqueous electrolytes. Consequently, our work provides a simple yet pragmatic approach to developing low-cost, low-toxic, high-power and high-energy-density aqueous batteries, not just for Li^+ but also for other batteries that are suffering from either severe hydrogen evolution reaction or high-resistance passivation film, such as zinc aqueous batteries (see Fig. S13).

Declaration of competing interest

The authors declare that they have no known competing financial interests or personal relationships that could have appeared to influence the work reported in this paper.

Acknowledgments

This work was supported by the Westlake Education Foundation and National Natural Science Foundation of China (21975207). The authors thank Westlake Instrumentation and Service Centers for Physical Sciences and Westlake Center for Micro/Nano Fabrication for characterization support and Westlake HPC Center for computation support.

Appendix A. Supplementary data

Supplementary data to this article can be found online at https://doi.org/10.1016/j.jechem.2022.10.033.

References

[1] H. Kim, J. Hong, K.Y. Park, H. Kim, S.W. Kim, K. Kang, Chem. Rev. 114 (2014) 11788–11827.
[2] J. Huang, Z. Guo, Y. Ma, D. Bin, Y. Wang, Y. Xia, Small Methods 3 (2019) 1800272.
[3] Y. Yamada, J. Wang, S. Ko, E. Watanabe, A. Yamada, Nat. Energy 4 (2019) 269–280.
[4] L. Suo, O. Borodin, T. Gao, M. Olguin, J. Ho, X. Fan, C. Luo, C. Wang, K. Xu, Science 350 (2015) 938–943.
[5] L. Suo, O. Borodin, W. Sun, X. Fan, C. Yang, F. Wang, T. Gao, Z. Ma, M. Schroeder, A. von Cresce, S.M. Russell, M. Armand, A. Angell, K. Xu, C. Wang, Angew. Chem. Int. Ed. Engl. 55 (2016) 7136–7141.
[6] F. Wang, O. Borodin, M.S. Ding, M. Gobet, J. Vatamanu, X. Fan, T. Gao, N. Eidson, Y. Liang, W. Sun, S. Greenbaum, K. Xu, C. Wang, Joule 2 (2018) 927–937.
[7] Y. Yamada, K. Usui, K. Sodeyama, S. Ko, Y. Tateyama, A. Yamada, Nat. Energy 1 (2016) 16129.
[8] R. Lin, C. Ke, J. Chen, S. Liu, J. Wang, Joule 6 (2022) 399–417.
[9] J. Chen, J. Vatamanu, L. Xing, O. Borodin, H. Chen, X. Guan, X. Liu, K. Xu, W. Li, Adv. Energy Mater. 10 (2019) 1902654.
[10] D. Chao, S.-Z. Qiao, Joule 4 (2020) 1846–1851.
[11] X. He, B. Yan, X. Zhang, Z. Liu, D. Bresser, J. Wang, R. Wang, X. Cao, Y. Su, H. Jia, C.P. Grey, H. Frielinghaus, D.G. Truhlar, M. Winter, J. Li, E. Paillard, Nat. Commun. 9 (2018) 5320.
[12] M.R. Lukatskaya, J.I. Feldblyum, D.G. Mackanic, F. Lissel, D.L. Michels, Y. Cui, Z. Bao, Energy Environ. Sci. 11 (2018) 2876–2883.
[13] P. Jiang, L. Chen, H. Shao, S. Huang, Q. Wang, Y. Su, X. Yan, X. Liang, J. Zhang, J. Feng, Z. Liu, ACS Energy Lett. 4 (2019) 1419–1426.
[14] H. Bi, X. Wang, H. Liu, Y. He, W. Wang, W. Deng, X. Ma, Y. Wang, W. Rao, Y. Chai, H. Ma, R. Li, J. Chen, Y. Wang, M. Xue, Adv. Mater. 32 (2020) e2000074.
[15] J. Xie, Z. Liang, Y.C. Lu, Nat. Mater. 19 (2020) 1006–1011.
[16] X. Yang, M. Jiang, X. Gao, D. Bao, Q. Sun, N. Holmes, H. Duan, S. Mukherjee, K. Adair, C. Zhao, J. Liang, W. Li, J. Li, Y. Liu, H. Huang, L. Zhang, S. Lu, Q. Lu, R. Li, C. V. Singh, X. Sun, Energy Environ. Sci. 13 (2020) 1318–1325.
[17] Z. Fang, Y. Luo, H. Liu, Z. Hong, H. Wu, F. Zhao, P. Liu, Q. Li, S. Fan, W. Duan, J. Wang, Adv. Sci. 8 (2021) e2100736.
[18] L. Carbone, M. Gobet, J. Peng, M. Devany, B. Scrosati, S. Greenbaum, J. Hassoun, J. Power Sources 299 (2015) 460–464.
[19] R. Marom, O. Haik, D. Aurbach, I.C. Halalay, J. Electrochem. Soc. 157 (2010) A972–A983.
[20] A. Naji, J. Ghanbaja, P. Willmann, D. Billaud, Carbon 35 (1997) 845–852.
[21] J. Tarascon, D. Guyomard, Solid State Ionics 69 (1994) 293–305.
[22] G. Pistoia, J. Electrochem. Soc. 118 (1971) 153–158.
[23] A.W. Knight, N.G. Kalugin, E. Coker, A.G. Ilgen, Sci. Rep. 9 (2019) 8246.
[24] K. Xu, A. von Cresce, U. Lee, Langmuir 26 (2010) 11538–11543.
[25] K. Xu, Chem. Rev. 114 (2014) 11503–11618.
[26] K. Chen, Z. Yu, S. Deng, Q. Wu, J. Zou, X. Zeng, J. Power Sources 278 (2015) 411–419.
[27] N. Takami, H. Inagaki, Y. Tatebayashi, H. Saruwatari, K. Honda, S. Egusa, J. Power Sources 244 (2013) 469–475.
[28] K. Qian, L. Tang, M. Wagemaker, Y.B. He, D. Liu, H. Li, R. Shi, B. Li, F. Kang, Adv. Sci. 4 (2017) 1700205.
[29] M. Uhlemann, M. Madian, R. Leones, S. Oswald, S. Maletti, A. Eychmuller, D. Mikhailova, ACS Appl. Mater. Interfaces 12 (2020) 37227–37238.

[30] N. Umirov, Y. Yamada, H. Munakata, S.-S. Kim, K. Kanamura, J. Electroanal. Chem. 855 (2019).
[31] C. Kim, N.S. Norberg, C.T. Alexander, R. Kostecki, J. Cabana, Adv. Funct. Mater. 23 (2013) 1214–1222.
[32] H.-J. Hong, S.-Y. Lee, S. Kwon, B.-S. Kim, S. Yoon, I.-S. Park, J. Alloy. Compd. 886 (2021).
[33] T. Zheng, J. Xiong, B. Zhu, X. Shi, Y.-J. Cheng, H. Zhao, Y. Xia, J. Mater. Chem. A 9 (2021) 9307–9318.
[34] S. Bhuvaneswari, U.V. Varadaraju, R. Gopalan, R. Prakash, Electrochim. Acta 301 (2019) 342–351.
[35] J. Abou-Rjeily, I. Bezza, N.A. Laziz, C. Autret-Lambert, M.T. Sougrati, F. Ghamouss, Energy Storage Materials 26 (2020) 423–432.
[36] W. Huang, G. Wang, C. Luo, Y. Xu, Y. Xu, B.J. Eckstein, Y. Chen, B. Wang, J. Huang, Y. Kang, J. Wu, V.P. Dravid, A. Facchetti, T.J. Marks, Nano Energy 64 (2019).
[37] X. Li, S. Hao, Z. Wang, C. Zhao, Z. Wang, Appl. Surf. Sci. 599 (2022).
[38] A. Tron, Y.D. Park, J. Mun, J. Power Sources 325 (2016) 360–364.
[39] S. Sundararajan, A. Kumar, B.C. Chakraborty, A.B. Samui, P.S. Kulkarni, Sustain, Energy Fuels 2 (2018) 688–697.
[40] A. Nandi, C. Ghosh, S. Basu, Nanoscale Adv. 1 (2019) 4965–4971.
[41] Y. Wang, T. Wang, D. Dong, J. Xie, Y. Guan, Y. Huang, J. Fan, Y.-C. Lu, Matter 5 (2022) 162–179.
[42] X. Lu, R.J. Jimenez-Rioboo, D. Leech, M.C. Gutierrez, M.L. Ferrer, F. Del Monte, ACS Appl. Mater. Interfaces 12 (2020) 29181–29193.
[43] Y. Shang, N. Chen, Y. Li, S. Chen, J. Lai, Y. Huang, W. Qu, F. Wu, R. Chen, Adv. Mater. 32 (2020) e2004017.
[44] J. Xu, X. Ji, J. Zhang, C. Yang, P. Wang, S. Liu, K. Ludwig, F. Chen, P. Kofinas, C. Wang, Nat. Energy. 7 (2022) 186–193.
[45] D. Dong, J. Xie, Z. Liang, Y.-C. Lu, ACS Energy Lett. 7 (2021) 123–130.